Decrease of L-band SAR backscatter with biomass of dense forests

Stéphane Mermoz[a], Maxime Réjou-Méchain[b,c,d], Ludovic Villard[a], Thuy Le Toan[a], Vivien Rossi[d,e], Sylvie Gourlet-Fleury[d]

[a] *Centre d'Études Spatiales de la BIOsphère, UMR CNRS 5126, University of Paul Sabatier, Toulouse, France*
[b] *Laboratoire Évolution et Diversité Biologique, UMR CNRS 5174, University of Paul Sabatier, Toulouse, France*
[c] *Institut de Recherche et Développement, UMR AMAP, F-34000 Montpellier, France*
[d] *Centre International de Recherche Agronomique pour le Développement, UR BSEF, Montpellier, France*
[e] *University of Yaoundé 1, UMI209 UMMISCO, Yaoundé, Cameroon*

Abstract

Synthetic aperture radar (SAR) is one of the most promising remote sensors to map forest carbon. The unique spaceborne and long- wavelength SAR data currently available are L-band data, but their relationship with forest biomass is still controversial, particularly for high biomass values. While many studies assume a complete loss of sensitivity above a saturation point, typically around 100 t.ha^{-1}, others assume a continuous positive correlation between SAR backscatter and biomass. The objective of this paper is to revisit the relationship between L-band SAR backscatter and dense tropical forest biomass for a large range of biomass values using both theoretical and experimental approaches. Both approaches revealed that after reaching a maximum value, SAR backscatter correlates negatively with forest biomass. This phenomenon is interpreted as a signal attenuation from the forest canopy as the canopy becomes denser. This result has strong implications for L-band vegetation mapping because it can lead to a greater-than-expected under-estimation of biomass. The consequences for L-band biomass mapping are illustrated, and solutions are proposed.

Keywords: Tropical forest, Carbon mapping, ALOS PALSAR.

1. Introduction

Forests act as both carbon sources and sinks through deforestation, degradation (Harris et al., 2012) and regrowth (Lewis et al., 2009). The monitoring of forest carbon stocks is a pressing concern to quantify the exchange of carbon between the surface and the atmosphere and therefore to reduce the uncertainty in the global carbon budget. Our knowledge of the distribution and amount of forest carbon is mostly based on ground measurements with relatively small field plots, which are not necessarily representative of their surrounding areas (Réjou-Méchain et al., 2014) and not uniformly distributed over forested areas and biomes (Gibbs et al., 2007; Houghton et al., 2009). Thus, most estimates of emissions from deforestation are based on a handful of biome-average datasets where a single representative value of forest carbon per unit area is applied to broad forest categories or biomes (Fearnside, 2000; Houghton, 1999; DeFries et al., 2002; Achard et al., 2002, 2004; Ramankutty et al., 2007). Such approaches have led to strong inconstancies between studies.

Remote sensing approaches offer considerable potential in support of forest monitoring as they provide long-term and repetitive observations over large areas. Standard optical data, such as provided by Landsat, are not sensitive to AGB beyond the canopy closure. However, using very high resolution optical data, the canopy texture can be characterised and then used to infer the above ground biomass (AGB) based on, for example, the Fourier-FOTO algorithm (Couteron, 2002; Couteron et al., 2005). A few studies have successfully used such an approach to map AGB in high biomass areas, such as Proisy et al. (2007) in two mangroves areas in French Guiana, Ploton et al. (2012) in a wet evergreen forest in India and Bastin et al. (In press) in a moist forest area in the Democratic Republic of the Congo. These three studies showed that AGB can be retrieved with no signal saturation and with a relative error ranging from 15 to 17%. However, these studies are performed at local scale and are limited to the small imaging swaths (maximum of 15×15 km). The large scale application of the methods is limited by the data cost and the temporal consistency of data due to cloud cover.

At the landscape scale, airborne LiDAR data-based approaches have proven to be accurate enough to infer the canopy height and structure, and thus to map the forest AGB at a high spatial resolution. In a recent meta-analysis, Zolkos et al. (2013) showed that the AGB can be retrieved with an error of 10% if the calibration is done using 1-ha plots. However, the cost of airborne LiDAR campaigns limits its use for large regions (however, see Mascaro et al. (2014)), and airborne campaigns are not feasible throughout the tropics for logistical and political reasons. Meanwhile, spaceborne LiDAR data are currently limited by discontinuous coverage and clouds (Lefsky et al., 2005; Baghdadi et al., 2013), and the derived large scale AGB products have low spatial resolution (1 km in Saatchi et al. (2011) and 500 m in Baccini et al. (2012)). In a recent contribution, Mitchard et al. (2013) used a large network of field plots in Amazonia to show that the uncertainties of Saatchi and Baccini's maps were far larger than expected, with over- and under-estimations greater than 25%.

Synthetic aperture radar (SAR) is one of the most promising remote sensors to map the global forest AGB. Many studies have shown that long-wavelength radar data are sensitive to AGB. Research efforts based on air-borne data and/or electromagnetic (EM) modelling have demonstrated that P-band data may be used for a larger range of AGB values than L-band data and thus should be privileged in forests with high biomass density (Le Toan et al., 1992). The first P-band SAR satellite, BIOMASS, will be launched approximately 2020 and will provide multi-temporal global forest AGB maps (Le Toan et al., 2011; ESA, 2012). Currently, the L-band ALOS PALSAR data acquired up to 2011 can be used to estimate the forest AGB, as well as its sequel, ALOS-2, launched in May 2014.

The L-band has been extensively used to estimate forest AGB (Santos et al., 2002; Santoro, 2003; Saatchi et al., 2011; Cartus et al., 2012; Carreiras et al., 2013), based on a positive correlation between SAR backscatter and in situ AGB. However, contrasting results have been yielded concerning the range of biomass that can be retrieved. Literature results suggest that there is an AGB level above which there is a loss of sensitivity between the L-band backscatter and AGB (Imhoff, 1995), commonly called the saturation phenomenon. The saturation level using HV polarization has been found to range between 40 and 150 $t.ha^{-1}$ (Dobson et al., 1992; Le Toan et al., 2004; Saatchi et al., 2007; Sandberg et al., 2011), reaching in some studies more than 250 $t.ha^{-1}$ (Hoekman and Quiriones, 2000; Lucas et al., 2010).

Questions can arise about the relationship between L-band backscatter and forest AGB beyond the saturation region. Many studies used a sigmoid function to describe the relationship between radar backscatter and AGB (Mitchard et al., 2011; Mermoz et al., 2014) to represent the 'saturation' behaviour. Some studies suggested that the sensitivity to AGB can be observed up to 400 t.ha^{-1} (Shugart et al., 2010; Morel et al., 2011; Hamdan et al., 2011; Englhart et al., 2011) and even 1000 t.ha^{-1} (Viergever, 2008; Mitchard et al., 2009). This finding is attributable to the use of a logarithmic (i.e., non-asymptotic) function to fit the experimental data, even though the positive correlation between SAR backscatter and AGB is usually not observed after 150-200 t.ha^{-1}. In addition to modelling results based on EM simulations (Villard, 2009), one study reported a decreasing trend after 200 t.ha^{-1} (Lucas et al., 2007) over dense mangrove forests in Australia, French Guyana and Malaysia, as well as another recent study over a forest-savanna mosaic in Cameroon (Mermoz et al., 2014). When retrieving AGB, the choice of the function describing the relationship between radar backscatter and AGB is crucial in the higher AGB range (i.e., $>$ 100-150 t.ha^{-1}) because it can lead to serious over- or under-estimation.

The objective of this paper is to revisit the relationship between L-band SAR backscatter and forest biomass for a large range of AGB values using both theoretical and experimental approaches. The focus is put on the high biomass range, for which the predicted AGB values may vary substantially between studies. The emphasis is on the tropical forests for which the carbon stocks and spatial distribution of carbon are poorly known despite containing 40 to 50 % of the land terrestrial carbon stocks. The following section introduces the theoretical approach. Section 3 provides informations on the study site and the field and SAR data. Section 4 describes the experimental approach, and section 5 discusses the results.

2. Theoretical Approach

2.1. Electromagnetic modelling to simulate forest backscatter at L-band

We aimed to model the backscatter at L-band from dense canpy forests as a function of AGB to investigate and physically explain their relationship. In this work, it is not intended that the dense canopy simulated by the model represents in detail the forest observed experimentally. Simulations were achieved from a discrete description of the forest canopy, using canonical shapes such as cylinders for the scatterers (Figure 1).

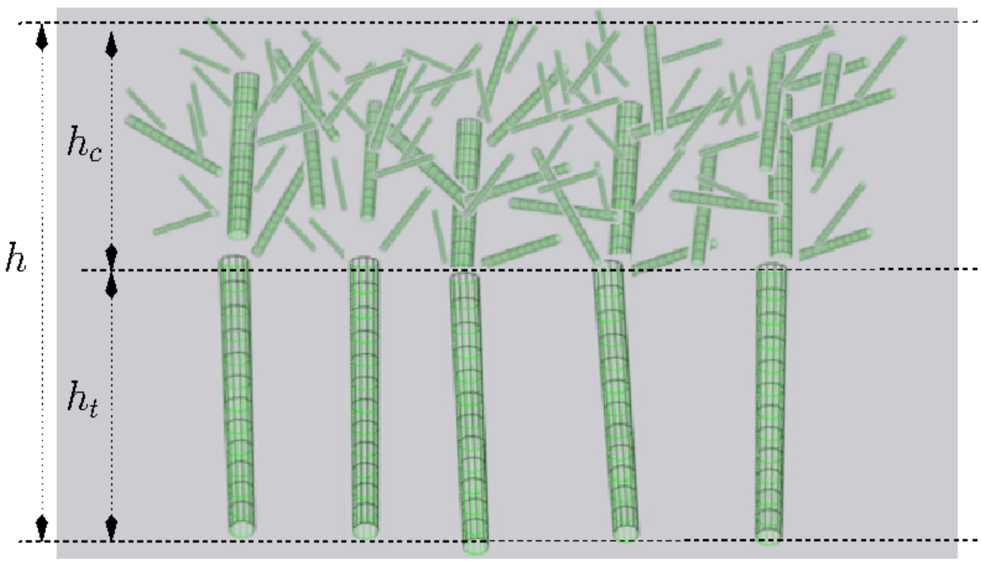

Figure 1: Illustration of the two-layered forest model. Vegetation scatterers are modelled by dielectric cylinders with various height and radius and are gathered into two horizontal layers. h is the total tree height, h_t is the trunk height and h_c is the crown height.

The vegetation scatterers are modelled by four classes of dielectric cylinders with varying height and radius and gathered into horizontal layers according to the spatial statistical distribution of their classes. Each of the four classes of cylinders are defined by the Gaussian distributions of their height and radius and by specific distributions for the Euler angles driving their 3D orientation. Following a Monte-Carlo process, these geometrical parameters are drawn for each cylinder to compute their scattering contribution. On the contrary, the mean extinction coefficient associated with each layer is an averaged (integral) expression according to the Foldy-Lax formulation (Ishimaru, 1978). Following the Distorted Born Wave Approximation, the total backscatter is deduced from the coherent sum (preserving the geometric and proper phase) of each scatterer contribution. The most important scattering mechanisms arise from direct contributions from scatterers belonging to the vegetation layers and the ground and from their coupling through the so-called double bounce scattering mechanism. These simulations were run through the MIPERS (Multistatic Interferometric Polarimetric ElectroMagnetic) model (Villard, 2009).

The geometrical parameters describing the modelled forest, required by the EM simulations, need to be derived. A forest growth model has been developed to deduce all the geometrical parameters from a chosen AGB, ranging from 50 to 450 $t.ha^{-1}$ with 50 $t.ha^{-1}$ steps. Based on the allometric relationships, the main steps of the forest growth model have been synthesized in Figure 2 and detailed in Appendix A. Because our field dataset (see section 3.2) lacked tree height measurements, we selected allometric relationships from the literature. We chose the allometric relationships given in Asner et al. (2012) based on 130 tropical forest field plots of 0.28 ha from Peru. The study from Asner et al. (2012) is of greatest interest for our purpose because it involves LiDAR mean canopy height (MCH), which fits the heights of our layered forest model better than tree height, which is more common in forest ecology. The allometric equations in Asner et al. (2012) were also detailed enough (including the relationship between tree height and biomass, between diameter and tree height and between basal area and tree height) to derive the inputs of the EM model.

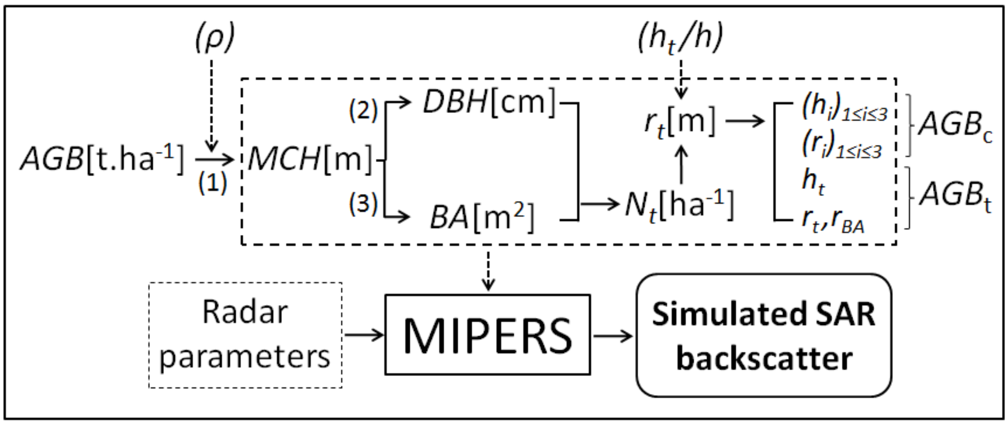

(1) $b_1.\ln(MCH) = \ln(0.5.AGB/a)$

(2) $BA = b_1.MCH$

(3) $\ln(h) = a + b_1 ln(DBH) + b_2(ln(DBH))^2 + b_3(ln(DBH))^3$

Figure 2: The forest growth model for deriving all the geometrical parameters required for the electromagnetic (EM) calculations. Equations (1), (2) and (3) relate mean canopy height (MCH) and above ground biomass (AGB), diameter at breast height (DBH) and MCH, and basal area (BA) and h, respectively

It is important to note that this approach targets a tropical type of forest but could be valid for various types of forests with dense canopy and radar frequencies, though some specific parameterizations would be required.

2.2. Results and Discussion

The resulting backscatter coefficient at HV polarization is plotted in green as a function of AGB in Figure 3. We can observe the increasing log shape followed by a slightly linear decrease after the highest value of backscatter (the decrease in magnitude is 0.9 dB between AGB from 230 $t.ha^{-1}$ to 450 $t.ha^{-1}$). To better understand the causes of the backscatter decrease, the backscatter coefficient at HV polarization is also derived by neglecting the attenuation from the vegetation. The so-called free-space (or no attenuation) backscatter is plotted in cyan in Figure 3, whereas the total attenuation, accounting for the signal loss (in dB) due to the wave propagation forth and back, is plotted at horizontal (red) and vertical (blue) polarizations. The decreasing backscatter plotted in green results from the saturation of the no-attenuation backscatter (the backscatter does not increase anymore with the number of scatterers and saturates), while the attenuation still increases with forest AGB. These simulations demonstrate that the antagonistic behaviours of no-attenuation backscatter and attenuation explain the negative correlation between L-band backscatter and high forest AGB.

The sensitivity of backscatter to AGB was found to be weak after the highest value of backscatter. To experimentally observe the decreasing trend of the backscatter, the analyses require reducing as much as possible the perturbing factors effects, which are related to the forest structure and environment, to the uncertainties in the radar data and in situ AGB data and to the misalignment in the locations of the radar and in situ observation geometries.

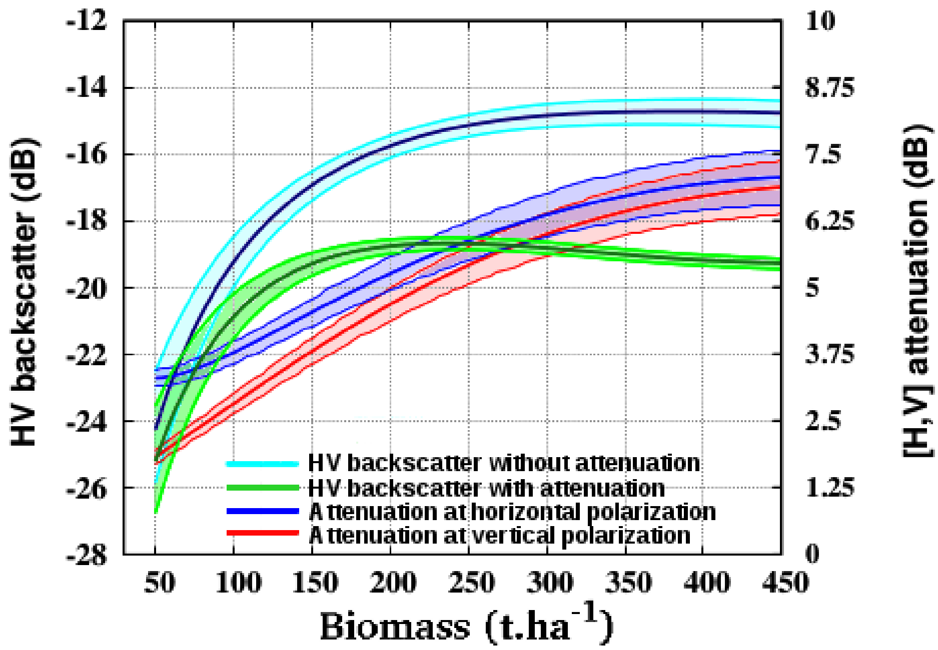

Figure 3: (Left axis) Simulated HV backscatters versus AGB, plotted in green (with attenuation from the vegetation) and cyan (without attenuation from the vegetation). (Right axis) Simulated attenuations, accounting for the signal loss (in dB) due to the wave propagation forth and back, at horizontal (red) and vertical (blue) polarizations. The uncertainties related to wood density (mean value of 0.58 g/cm^3) are represented by the filled colour domains surrounding the curves.

3. DATA

3.1. Study area

The study area shown in Figure 4 covers 8,300 km^2 in the southwestern Central African Republic (CAR), from 3^o26N to 4^o36N and from 15^o08E to 17^o48E. The climate is tropical humid with a mean annual rainfall of 1300-1600 mm (Hijmans et al., 2005). The altitude ranges from approximately 400 to 800 m (Boulvert, 1987). Our study area is mostly covered with semievergreen rain forests from the Guineo-Congolian region with locally flooded or swamp forests, savannas located north of the Congo basin and forest-enclosed savannas.

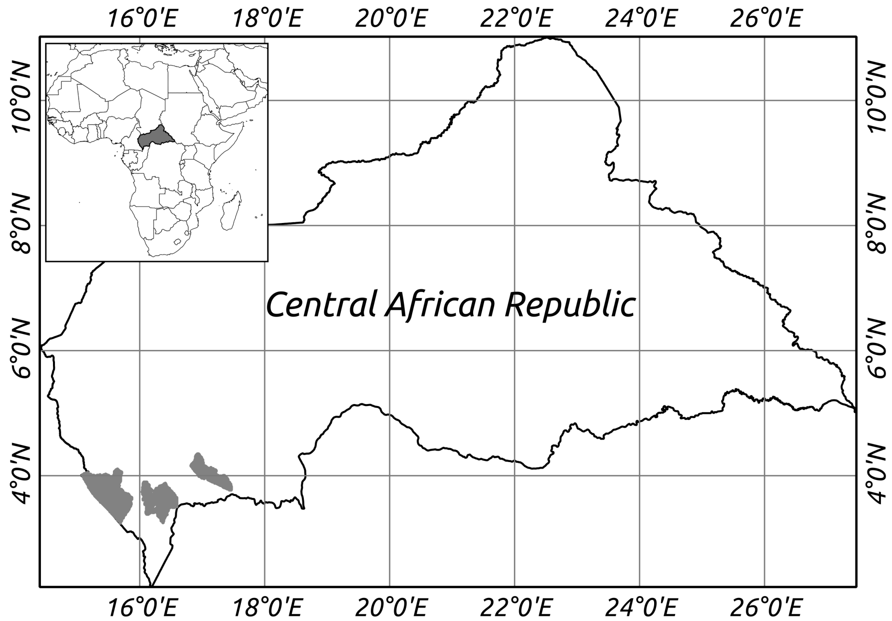

Figure 4: Map of the Central African Republic showing in grey the location of the forest concessions targeted for the study.

3.2. Field data

3.2.1. Description of field data

The forestry data were extracted from commercial forest inventories conducted by four logging companies: IFB (Industrie Forestière de Batalimo) in 1993-1996, SCAF (Société CentrAfricaine Forestière), SOFOKAD (Société Forestière de la Kadéi) and TCA (Thanry CentrAfrique) in 2005-2006. These companies benefited from financial and technical support from the French-funded programs ECOFAC (IFB) and PARPAF (SCAF, SOFOKAD, and TCA), which considerably increased the quality of the data collected. The four companies followed the same standardized inventory protocol fully described in Réjou-Méchain et al. (2011). This protocol consisted of continuous transects 25-m wide and 2 to 3 km apart and subdivided into rectangular 25-m wide by 200-m long (i.e., 0.5-ha) field plots. In the northwestern area of the IFB concession, the plots were non-adjacent but the transects were closer (i.e., with a similar sampling intensity). Overall, 19,584 plots were inventoried by the four companies.

Trees with a diameter at breast height (DBH) $\geq$ 30 cm were recorded within each 0.5-ha field plot, while those between 10 and 30 cm DBH were recorded on a 0.1 (IFB) or 0.125 ha sub-plot area. The trees were allocated into 10-cm wide DBH classes. All the trees were identified whenever possible to the species level through either commercial or local names and then converted into scientific names. Such a protocol proved devoid of major bias in the identification of floristic patterns compared to extensive botanical controls (Réjou-Méchain et al., 2011). Overall, 2,401,016 trees were recorded and the taxonomy was revised and homogenized using the African Flowering Plants Database and the Angiosperm Phylogeny Group III for orders and families (Bremer et al., 2009).

3.2.2. Field AGB estimation

The successive steps for AGB calculation are summarised in Figure 5 and fully described in Appendix B. Because the trees were allocated into diameter classes during the inventories, we first modelled the diameter distribution of the trees using a truncated exponential function. According to its diameter class, each tree was assigned a DBH drawn randomly from this exponential distribution. Because height-diameter allometries can vary from one region to another, we used the central African Weibull-H model from Feldpausch et al. (2012) to estimate the tree height from DBH. We assigned a wood specific gravity value (WSG; i.e., wood density) to each tree based on its taxonomy using the WSG dataset of Gourlet-Fleury et al. (2011).

The AGB was then estimated using the moist pantropical equation from Chave et al. (2005). Finally, the AGB density ($t.ha^{-1}$) was estimated for each 0.5-ha field plot by summing the tree AGBs of all individuals with a higher expansion factor (8 or 10) for trees between 10 and 30 cm DBH (these trees were sampled in a fifth or a quarter of the 0.5-ha plots). During all the steps, we propagated the errors associated with the diameter assignment, the height estimation, the wood specific gravity estimation, and the AGB model thanks to the Monte Carlo simulations (1000 iterations).

3.3. SAR data

Six ALOS PALSAR mosaics (five paths) with 25-m resolution over the study area (latitudes from 3 to 5^o and longitudes from 15 to 18^o), acquired from 4 July to 12 November 2007, were supplied by JAXA. One unit mosaic data contains one degree latitude-longitude geographical unit. The signal was converted into γ^o values using the following equation:

$$\gamma^o = 10.log_{10}(DN^2) + CF \quad (1)$$

where DN stands for digital number and CF is a calibration factor described in Shimada et al. (2009). The data have been processed by JAXA

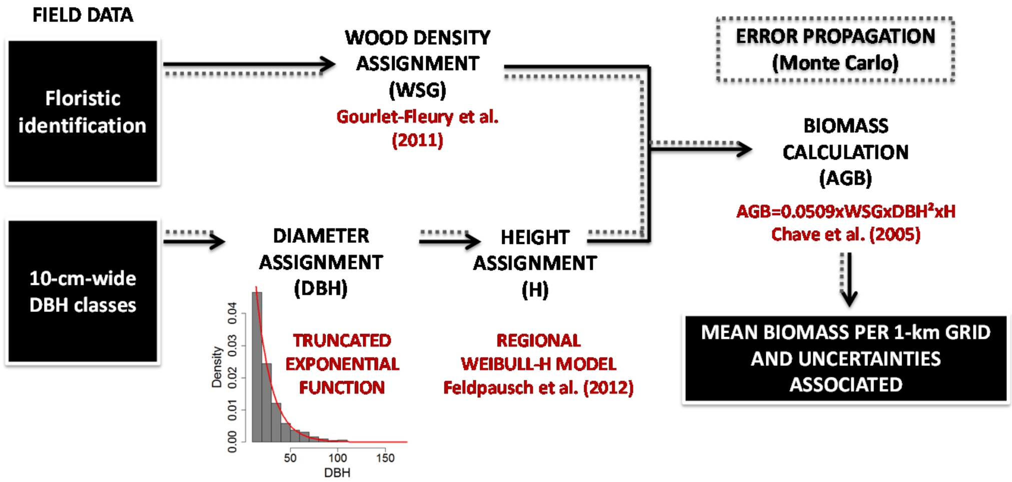

Figure 5: Summary of the successive steps for above ground biomass (AGB) calculation.

using the large-scale mosaicking algorithm from Shimada and Ohtaki (2010). It includes ortho-rectification, slope correction and radiometric calibration between neighbouring strips. The slope correction accounts for the variations in the ground scattering area and the local incidence angle. The method precisely calculates the illumination area from the Shuttle Radar Topography Mission (SRTM) digital elevation model (DEM) and applies a correction factor to the backscattering coefficient based on the local incidence angle. The radiometric calibration between two neighbouring strips is performed by comparing the intensities of small coregistered image chips that are extracted from the overlapped region from half of each of the far and near ranges. The resulting gain and offset are used to correct the two neighbouring strips. Note that these methods, which are optimized to reduce backscatter mismatches among adjacent paths, can introduce modifications of the backscatter that might hamper AGB retrieval.

The equivalent number of looks (ENL) for the ALOS-PALSAR data was 16 after these pre-processing steps. The six images were then geolocated (latitude/longitude coordinates were assigned to each pixel) using the coordinates of the four image corners and mosaicked. The terrain slopes were derived from the SRTM DEM with approximately 90 m resolution.

4. Experimental Approach

4.1. Reduction of the uncertainties

To test whether the signal attenuation found in section 2 experimentally occurs in dense forests, we reduced the perturbing factor effects as much as possible. The estimation of radar backscatter at the pixel basis is mainly affected by the speckle noise, which is modelled as multiplicative noise and depends on the ENL. To reduce the effects of speckle noise, we degraded the PALSAR resolution within a 1-km resolution grid by averaging the pixels, and we averaged the field plots, leading to upscaled plots, to the same 1-km grid. The resulting ENL of the ALOS-PALSAR data, estimated by dividing the square of the mean backscatter intensity by the corresponding variance over a set of homogeneous areas, was $> 2,000$.

The perturbing effects linked to in situ observation geometry include the plot size, tree canopy layover and border effects, errors in data geolocation and topographic effects. We discarded the upscaled plots that contained less than two 0.5-ha field plots. The remaining upscaled plots contained a mean field plot size of 2.1 ± 0.6 ha and were all ≥ 1 ha, which may correspond to an AGB estimation sampling error less than 17% according to Réjou-Méchain et al. (2014). Then, we attempted to optimise the representativeness of the ground information in the whole 1-km pixels and selected the pixels that were likely to contain homogeneous forests. We calculated the coefficient of variation (CV) of the AGB among the field plots within each upscaled plot and filtered out upscaled plots with a CV > 0.25. The forest under study has to be homogeneous enough to maximise the representativity of 1 ha or more of in situ AGB into 100 ha of forest. Therefore, we discarded upscaled plots with a standard deviation of the SAR backscatters > 0.75 dB. The latter thresholds were chosen as a compromise between the quality and the number of remaining observations (see Appendix C). It is interesting to note that the standard deviation of the SAR backscatters was highly correlated to the standard deviation of the terrain slope (i.e., the standard deviations were calculated from the original 25 m and 90 m subpixels within each 1-km pixel). The selection of pixels with low standard deviations of SAR backscatters therefore reduced topographical heterogeneities, which are a major driver of biomass heterogeneity (Réjou-Méchain et al., 2014) and a major source of uncertainties in radar backscattering (Van Zyl et al., 1993). Topographical effects were also reduced by discarding upscaled plots with a median of the slope $> 2^o$. This step ensured both higher forest homogeneity within the pixels and lower noise in the radar backscattering.

In the following, we assume that the backscatter saturation occurs for AGB of approximately 150 t.ha^{-1} (Mermoz et al., 2014) and we discarded the few upscaled plots with less than 150 t.ha^{-1} in the analyses.

When using multitemporal radar data, sources of noise include environment effects (soil moisture) and radar calibration. Temporal shifts between in situ and radar data acquisitions may also induce biases. In our study, the temporal variation of the backscatter signal was minimized because the upscaled plots used for the calibration were derived from ALOS images acquired from 4 July to 29 September 2007, i.e., during the wet season. The temporal difference between the radar data acquisition (2007) and the field surveys for in situ data (from 1993 to 2006) was rather important. A recent study conducted in the same study area by Gourlet-Fleury et al. (2013) in permanent plots monitored since 1982 showed a mean gain in AGB of 2.58 and 4.82 $t.ha^{-1}.yr^{-1}$ for the control and logged plots respectively. Thus, the largest expected AGB change between the field surveys and the radar data acquisition was 68 $t.ha^{-1}$. However, note that the oldest inventories, which were conducted in IFB, were located on poor sandy soils characterized by a pool of species with higher wood density and lower growth rates (Gourlet-Fleury et al., 2011; Fayolle et al., 2012; Réjou-Méchain et al., 2014). Thus, the largest AGB change of 68 $t.ha^{-1}$ is unlikely to occur in that area. In addition, the study area is not subject to large scale deforestation; thus, even if disturbances occurred within the pixel, this would probably lead to a large CV in the backscatter signal and our data quality filter would discard such a pixel.

Details on the effects of upscaled plot selection on the relationship between the radar backscatter and AGB are provided in Appendix C.

4.2. Empirical model calibration

The relationships between ALOS backscatters and field AGB were established using linear regressions. The Pearson coefficient of correlation r and the bias (in dB) were used to assess the quality of the fits. To assess the robustness of our model parameters, we used Monte Carlo simulations (n=1,000 simulations) where field AGB uncertainties were propagated to the calibration model. For each simulation, field AGB values were drawn randomly and independently from the normal distribution $\mathcal{N}(\mu_{AGB,plot}, \sigma_{AGB,plot})$ where $\mu_{AGB,plot}$ and $\sigma_{AGB,plot}$ are, respectively, the mean and the standard deviation of the field AGB within an upscaled plot (see Appendix B). At each simulation, the parameters of the linear regression between ALOS backscatters and field AGB were stored.

4.3. Results

SAR backscatter at HV polarization versus in situ AGB after the selection process are shown in Figure 6. The field dataset had 4,755 upscaled plots of 1 km^2 at HV polarization before the selection process and 632 after. The remaining in situ AGB have a mean of 312.3 t.ha^{-1} and range from 150.1 to 545.6 t.ha^{-1}. For illustration purposes, we added in Figure 6 1-ha field plot data, shown in red, acquired from the REDDAF project (Haeusler et al., 2012) in 2011 in the Adamawa Province, Cameroon and in 2013 in the Central Province, Cameroon. Sixteen savanna and 25 forest plots were surveyed. Only 1-ha plots with AGB below 150 t.ha^{-1} and slopes below 5^o were used, i.e., 21 savanna and 5 forest plots. The field data processing followed the methodology in Mermoz et al. (2014). The resolution used for these data is 1 ha (not 100 ha as with upscaled plots from the CAR).

The relationships in Figure 7, which is a zoom of the small window found in the right part of Figure 6 at HH and HV polarizations, show strong and significant negative correlations with AGB ($P < 0.0001$). The linear decrease observed in Figure 3 is well reproduced by the empirical approach. The best-fit linear regression at HH polarization, using 635 upscaled plots, was found

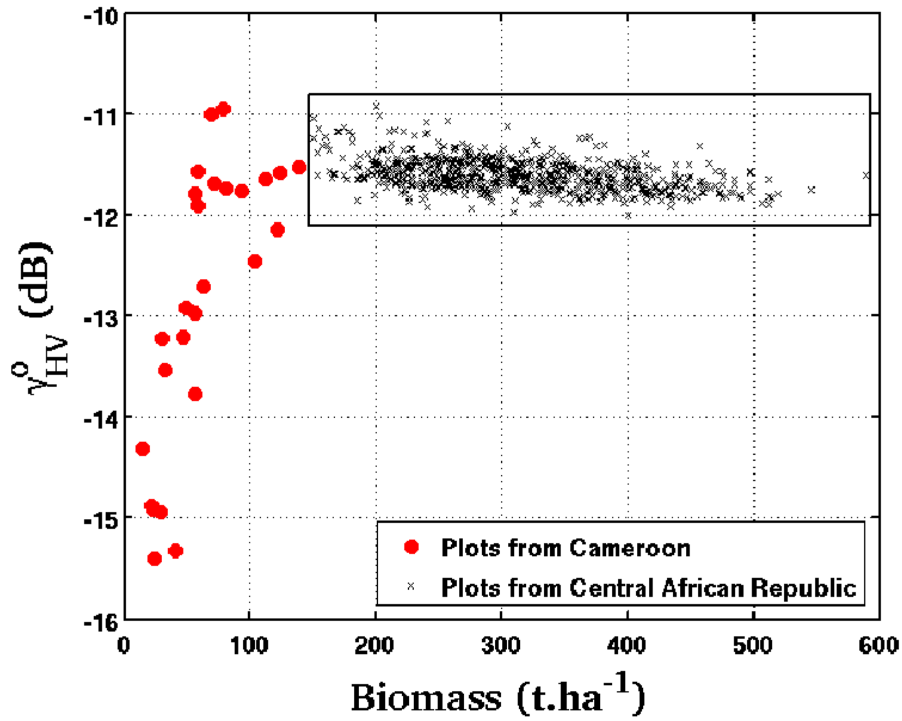

Figure 6: SAR backscatter at HV polarization versus in situ above ground biomass (AGB) after the selection process. Twenty-one savanna and 5 forest 1-ha field plots, acquired from the REDDAF project (Haeusler et al., 2012), in 2011 in the Adamawa Province, Cameroon and in 2013 in the Central Province, Cameroon, were added.

to be $\gamma^o_{HH} = -6.25 - 9.47.10^{-4} \times AGB$ with a Pearson's r of 0.47. The best-fit linear regression at HV polarization, using 632 upscaled plots, was found to be $\gamma^o_{HV} = -11.34 - 8.29.10^{-4} \times AGB$, with a r of 0.43. The straight lines corresponding to the linear regression models in Figure 7 are surrounded with the 95% confidence envelopes of the regression domains. The coefficients of correlation r at both polarizations were significantly higher than the critical value at the 2% risk for 632 plots, i.e. $r \simeq 0.1$. The backscatter γ^o_{HH} was more correlated to in situ AGB than γ^o_{HV}, and although the HH polarization is more sensitive to environmental error sources, such as soil moisture, γ^o_{HH} was not more biased than γ^o_{HV}. In addition, it is well known that the random error in the independent variable, such as the error that results from sampling errors in AGB, leads to a systematic underestimation of the slope in an ordinary least square regression, a bias referred to as regression dilution (Fuller, 1987; Réjou-Méchain et al., 2014). Thus, in this study, the attenuation has probably been under-estimated through a dilution effect in the regression parameters.

The field AGB uncertainties were propagated to the calibration model using a Monte Carlo scheme (n=1000 simulations) to assess the robustness of our model parameters. The mean slope was found to be $-9.47.10^{-4} \pm 1.38.10^{-6}$ and $-7.84.10^{-4} \pm 7.49.^{-5}$ at HH and HV polarizations respectively, and all the resulting slopes were negative. Therefore, the negative slopes are unlikely to be attributed to the field AGB uncertainties.

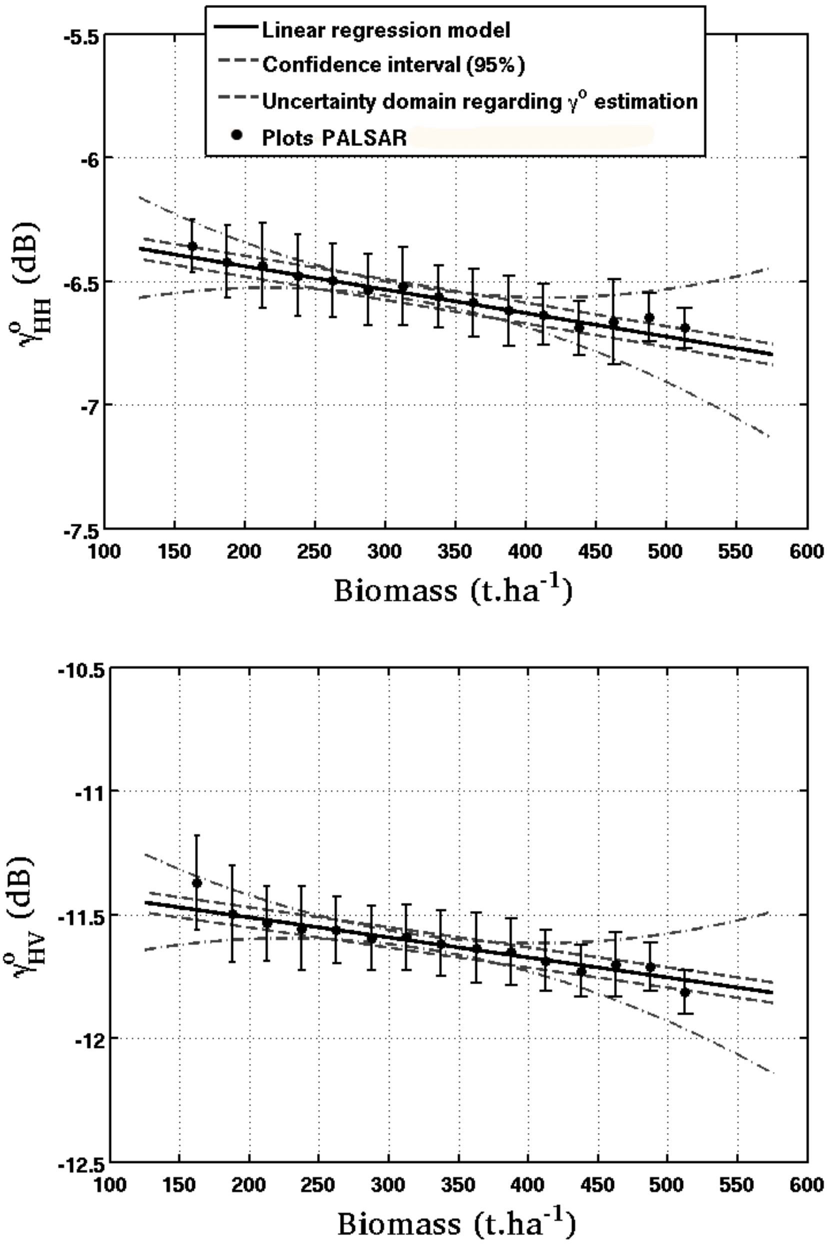

Figure 7: Backscattering coefficient γ^o versus in-situ above ground biomass (AGB) (zoom of the small window found in the right part of Figure 6). For illustration purposes, the dots are the mean values per 25 t.ha^{-1} biomass class and the bars are the standard deviations of points per 25 t.ha^{-1} biomass class. The linear regressions (black solid lines) were fitted to the individual upscaled plot data (see Figure 6). The observed correlations were Pearson's r of 0.47 and 0.43 at HH and HV polarizations respectively. The uncertainty domains regarding the backscatter estimation for a given AGB, related to the prediction interval from the linear model, are plotted in grey dash-dotted lines.

5. Discussion

The methodology often used for AGB mapping with the L-band is to apply the inverse model to all pixels having backscatter intensities less than the saturation point, and to assign an AGB value equal to the saturation point to the other pixels. First, the value of the saturation point should be identified clearly, which is highly difficult without numerous and accurate calibration points. Second, this approach can lead to a strong and systematic under-estimation of AGB, as illustrated by our results, because the backscatter of high biomass forests may be on average lower than the previously assumed signal saturation point. For example, 718 upscaled plots over the 1019 plots from the IFB concession have γ^o_{HV} below the maximum backscatter (-11.52 dB, corresponding to AGB of 150 t.ha^{-1}) of the model calibrated in Mermoz et al. (2014). If such an approach was implemented in the present study, the inversion of plots with in situ AGB of 200, 400 and 600 t.ha^{-1} would have given, on average, AGB estimates of 159.7, 95.6 and 79.7 t.ha^{-1}, respectively. The higher the AGB of the forest, the greater the AGB under-estimation by the inversion model. This phenomenon is illustrated in Figure 8 where AGB from Cameroon at 1 ha resolution and from the CAR at 1 km resolution are estimated from the model of Mermoz et al. (2014), which is dedicated to the estimation of AGB $<$ 150 t.ha^{-1}, and compared with field AGB.

The effect of the signal attenuation is illustrated in Figure 9, showing the AGB map over the SCAF concession that is obtained using the sigmoid model of Mermoz et al. (2014). Over an 11 km^2 area of mature dense forest, the mean AGB estimated in situ is 238 t.ha^{-1} (based on 9 upscaled plots with 2.5 ha mean size), whereas the mean AGB estimated by SAR is only

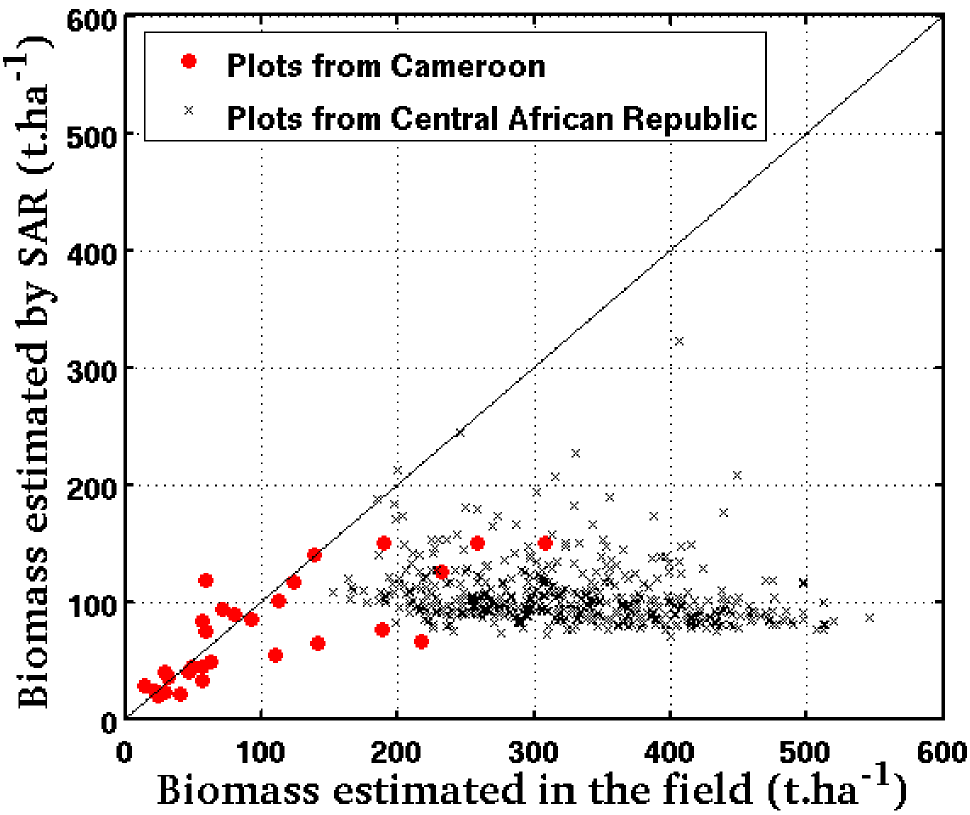

Figure 8: AGB from Cameroon at 1 ha resolution and from the Central African Republic (CAR) at 1 km resolution, estimated from the model of Mermoz et al. (2014), which is dedicated to the estimation of AGB < 150 t.ha^{-1}. The AGB > 150 t.ha^{-1} are strongly under-estimated.

109 t.ha^{-1}, a value far lower than the saturation point, e.g., 150 t.ha^{-1}. On the contrary, over an 11 km^2 area of early successional forest where the mean AGB estimated in situ is 88 t.ha^{-1} (based on 9 upscaled plots with 2.3 ha mean size), the SAR backscatters are unexpectedly high. The mean AGB estimated by SAR is therefore overestimated with 145 t.ha^{-1} (more than 91% of the pixels estimated by SAR are set up to the saturation point).

This extreme exemple shows that the SAR backscatter may be far higher over early successional forests than over mature forests, resulting in entirely inverted AGB patterns. It illustrates a strong decrease in backscatter with AGB. It is important to note that the high backscatter over early successional forests in this example is neither explained by wetness due to flooding nor by topography.

A major problem is that it is impossible to know based solely on backscatter intensities if a pixel should be inverted because it is below the maximum backscatter or should be discarded because it is above the maximum backscatter. The most straightforward solution is to use independent sources of information, such as land cover maps, to mask out dense forest areas as performed in Mermoz et al. (2014). For example, in Africa, land cover maps containing 'dense forest' classes have been recently achieved over a large part of the Congo Basin at 250 to 1000 m resolution (Vancutsem et al., 2009; Gond et al., 2013; Viennois et al., 2013) or over the entire Congo Basin at 300 to 1000 m resolution (Verhegghen et al., 2012). However, further sources of errors are associated with land cover maps (Morton et al., 2014) and may also impact the final AGB map. The products of forest canopy density (DiMiceli et al., 2011; Sexton et al., 2013) may also be used to assess the forest density and ensure a good application of the AGB model. Another highly conservative solution is to lower the maximum value of AGB that can be inferred from the inversion model, so that any backscatter value that would have been influenced by the attenuation effect is discarded. In the present study, the higher attenuation effect observed for field AGB > 150 $t.ha^{-1}$ led to an estimated value of 70.3 $t.ha^{-1}$. Thus, any map with a maximum value

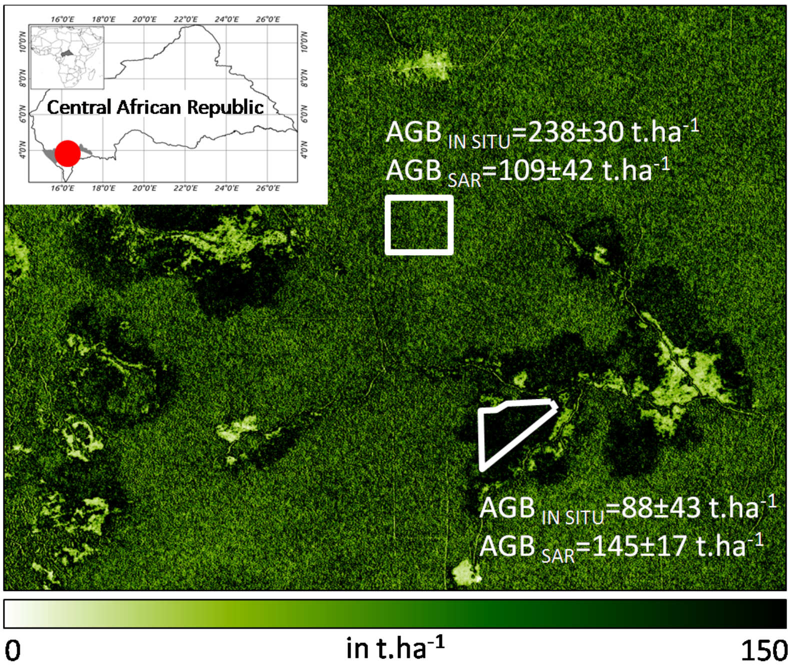

Figure 9: AGB map over a 1000 km^2 area centred on 3.70^{o}N and 16.45^o over the SCAF concession, that would be obtained using the model of Mermoz et al. (2014), which is dedicated to the estimation of AGB < 150 t.ha^{-1}. Over an 11 km^2 area of dense forest, the mean AGB estimated in situ is 238 t.ha^{-1} (based on 9 upscaled plots with 2.5 ha mean size), whereas the mean AGB estimated by SAR is only 109 t.ha^{-1}, a value far lower than the saturation point, e.g., 150 t.ha^{-1}, and the field-based estimate. Over an 11 km^2 area of young forest, the mean AGB estimated in situ is 88 t.ha^{-1} (based on 9 upscaled plots with 2.3 ha mean size), whereas the mean AGB estimated by SAR is 145 t.ha^{-1}. This example shows that SAR backscatter may be far higher over young forests than over old dense forests and illustrates the decrease in the backscatter with AGB.

of 70 t.ha^{-1} would be not affected by the attenuation effect.

We also illustrated in this study that a much accurate relationship between L-band backscatters and AGB values was observed when all the possible sources of errors were minimized. An adequate ground sampling strategy focusing on homogeneous areas in terms of radar backscattering and topography and avoiding steep areas will significantly reduce the errors associated with the calibration step (Réjou-Méchain et al., 2014). This is especially important if the maximum backscatter needs to be inferred accurately. However, this strategy should be weighed against the potential to bias the calibration model if forests in steep areas differ systematically in the relationship between the backscatter signal and biomass.

6. Conclusions

In the literature, there is a wide consensus that L-band backscatter intensity increases with AGB for small AGB values and subsequently saturates for larger values. In this study, we used both theoretical and experimental approaches to investigate the behaviour of L-band signals in dense forests. The theoretical modelling results proved that a backscatter decrease with AGB can occur in dense forests, resulting from the saturation of the free-space (or no attenuation) backscatter, while attenuation still increases with forest AGB. We then tested whether the signal attenuation experimentally occurs in dense forests and showed that the theoretical backscatter decrease was well reproduced by the experimental approach. The decrease in the backscatter can have strong implications for L-band vegetation mapping, such as severe biomass under-estimation and reversed patterns of AGB. Some solutions were proposed to counteract these effects.

As shown in this study, the L-band does not entirely lose sensitivity at large biomass values, suggesting that much progress can be made by refining our understanding of radar backscattering behaviour at L-band. Given the successful launch of ALOS2 in May 2014 and the future SAOCOM mission planned for launch in 2017, further works should test the generalization of the L-band's signal attenuation in other forest types, as Lucas et al. (2007) found in a mangrove forest. Our result could be, for example, strengthened by a validation in various study areas. Because large field datasets such as the one used in our study are extremely scarce, especially in the tropics, the recent AGB maps derived from high-resolution airborne LiDAR data (Asner et al., 2010) may constitute a good opportunity to test such signal attenuation. If our finding is generalized elsewhere, the backscatter decrease could be used as a new model for inferring high biomass values at 1km resolution over dense forests based on forest canopy density products. This would represent a novel approach and a major advance in the use of L-band SAR for AGB estimation.

7. Acknowledgements

The authors would like to thank Masanobu Shimada and his team from JAXA for providing the ALOS PALSAR data and for pre-processing the PALSAR mosaic data. We are grateful to the PARPAF project and the leading consortium CIRAD (Centre de coopération Internationale en Recherche Agronomique pour le Développement) and FRM (Fôret Ressources Management). We also address special thanks to the Ministère des Eaux, Forêts, Chasses et Pêches of Central African Republic and the four forest companies that provided access, albeit restricted, to their inventory data for research purposes. Stéphane Mermoz and Maxime Réjou-Méchain were recipients of postdoctoral grants from CNES (N^o 0101595 and 0101544, respectively). Maxime Réjou-Méchain was supported by two 'Investissement d'Avenir' grants managed by Agence Nationale de la Recherche (CEBA, ref. ANR-10-LABX-2501; TULIP, ref. ANR-10-LABX-0041) and by the CoFor-Tip project (ANR-12-EBID-0002).

8. References

References

Achard, F., Eva, H., Mayaux, P., Stibig, H., Belward, A., 2004. Improved estimates of net carbon emissions from land cover change in the tropics for the 1990s. Global Biogeochemical Cycles 18, GB2008.

Achard, F., Eva, H., Stibig, H., Mayaux, P., Gallego, J., Richards, T., Malingreau, J., 2002. Determination of deforestation rates of the world's humid tropical forests. Science 297, 999–1002.

Asner, G.P., Mascaro, J., Muller-Landau, H.C., Vieilledent, G., Vaudry, R., Rasamoelina, M., Hall, J.S., van Breugel, M., 2012. A universal airborne lidar approach for tropical forest carbon mapping. Oecologia 168, 1147–1160.

Asner, G.P., Powell, G.V., Mascaro, J., Knapp, D.E., Clark, J.K., Jacobson, J., Kennedy-Bowdoin, T., Balaji, A., Paez-Acosta, G., Victoria, E., et al.,

2010. High-resolution forest carbon stocks and emissions in the amazon. Proceedings of the National Academy of Sciences 107, 16738–16742.

Baccini, A., Goetz, S., Walker, W., Laporte, N., Sun, M., Sulla-Menashe, D., Hackler, J., Beck, P., Dubayah, R., Friedl, M., et al., 2012. Estimated carbon dioxide emissions from tropical deforestation improved by carbon-density maps. Nature Climate Change 2, 182–185.

Baghdadi, N., le Maire, G., Fayad, I., Bailly, J.S., Nouvellon, Y., Lemos, C., Hakamada, R., 2013. Testing different methods of forest height and aboveground biomass estimations from ICESat/GLAS data in eucalyptus plantations in Brazil .

Bastin, J.F., Barbier, N., Couteron, P., Adams, B., Shapiro, A., Bogaert, J., De Canniere, C., In press. Aboveground biomass mapping of african forest mosaics using canopy texture analysis: towards a regional approach. Ecological Applications .

Boulvert, Y., 1987. Carte oro-hydrographique de la République Centrafricaine (feuille ouest-feuille est) à 1:1 000 000. Editions de l'ORSTOM, Paris.

Bremer, B., Bremer, K., Chase, M., Fay, M., Reveal, J., Soltis, D., Soltis, P., Stevens, P., 2009. An update of the Angiosperm Phylogeny Group classification for the orders and families of flowering plants: APG III. Botanical Journal of the Linnean Society .

Carreiras, J., Melo, J.B., Vasconcelos, M.J., 2013. Estimating the aboveground biomass in miombo savanna woodlands (mozambique, east africa) using l-band synthetic aperture radar data. Remote Sensing 5, 1524–1548.

Cartus, O., Santoro, M., Kellndorfer, J., 2012. Mapping forest aboveground biomass in the Northeastern United States with ALOS PALSAR dual polarization L-band. Remote Sensing of Environment , 466–478.

Chave, J., Andalo, C., Brown, S., Cairns, M., Chambers, J., Eamus, D. Flster, H., 2005. Tree allometry and improved estimation of carbon stocks and balance in tropical forests. Oecologia , 87–99.

Couteron, P., 2002. Quantifying change in patterned semi-arid vegetation by fourier analysis of digitized aerial photographs. International Journal of Remote Sensing 23, 3407–3425.

Couteron, P., Pelissier, R., Nicolini, E.A., Paget, D., 2005. Predicting tropical forest stand structure parameters from fourier transform of very high-resolution remotely sensed canopy images. Journal of Applied Ecology 42, 1121–1128.

DeFries, R., Houghton, R., Hansen, M., Field, C., Skole, D., Townshend, J., 2002. Carbon emissions from tropical deforestation and regrowth based on satellite observations for the 1980s and 1990s. Proceedings of the National Academy of Sciences 99, 14256–14261.

DiMiceli, C., Carroll, M., Sohlberg, R., Huang, C., Hansen, M., Townshend, J., 2011. Annual global automated modis vegetation continuous fields (mod44b) at 250 m spatial resolution for data years beginning day 65, 2000–2010, collection 5 percent tree cover. University of Maryland, College Park .

Dobson, C., Ulaby, F., Ulaby, F., Le Toan, T., Beaudoin, A., Kasischke, E., Christensen, N., 1992. Dependence of radar backscatter on coniferous forest biomass. Geoscience and Remote Sensing, IEEE Transactions on 30, 412–415.

Englhart, S., Keuck, V., Siegert, F., 2011. Aboveground biomass retrieval in tropical forests. the potential of combined X-and L-band SAR data use. Remote sensing of environment 115, 1260–1271.

ESA, 2012. Report for Mission Selection:BIOMASS. Technical Report ESA SP-1324/1. European Space Agency, Noordwijk, The Netherlands.

Fayolle, A., Engelbrecht, B., Freycon, V., Mortier, F., Swaine, M., Réjou-Méchain, M., Doucet, J.L., Fauvet, N., Cornu, G., Gourlet-Fleury, S., 2012. Geological substrates shape tree species and trait distributions in african moist forests. PloS one 7, e42381.

Fearnside, P.M., 2000. Global warming and tropical land-use change: greenhouse gas emissions from biomass burning, decomposition and soils in forest conversion, shifting cultivation and secondary vegetation. Climatic change 46, 115–158.

Feldpausch, T., Lloyd, J., Lewis, S., Brienen, R., Gloor, E., Monteagudo Mendoza, A., Lopez-Gonzalez, G., Banin, L., Abu Salim, K., Affum-Baffoe, K., et al., 2012. Tree height integrated into pan-tropical forest biomass estimates. Biogeosciences Discussions 9, 2567–2622.

Fuller, W., 1987. Measurement Error Models. New-York : John Wiley.

Gibbs, H., Brown, S., Niles, J., Foley, J., 2007. Monitoring and estimating tropical forest carbon stocks: making REDD a reality. Environmental Research Letters 2, 045023.

Gond, V., Fayolle, A., Pennec, A., Cornu, G., Mayaux, P., Camberlin, P., Doumenge, C., Fauvet, N., Gourlet-Fleury, S., 2013. Vegetation structure and greenness in central africa from modis multi-temporal data. Philosophical Transactions of the Royal Society B: Biological Sciences 368, 20120309.

Gourlet-Fleury, S., Mortier, F., Fayolle, A., Baya, F., Ouedraogo, D., Bénédet, F., Picard, N., 2013. Tropical forest recovery from logging: a 24 year silvicultural experiment from central africa. Philosophical Transactions of the Royal Society B368: 20120302 .

Gourlet-Fleury, S., Rossi, V., Réjou-Méchain, M., Freycon, V., Fayolle, A., Saint-André, L., Cornu, G., Gerard, J., Sarrailh, J., Flores, O., et al., 2011. Environmental filtering of dense-wooded species controls above-ground biomass stored in african moist forests. Journal of Ecology 99, 981–990.

Haeusler, T., Gomez, S., Siwe, R., Le Toan, T., Mermoz, S., Schardt, M., Sannier, C., 2012. Reducing emissions from deforestation and degradation in africa (reddaf). 7th Research Framework Programme publication EU Publication: Lets embrace space 2, 118–125.

Hamdan, O., Aziz, H.K., Rahman, K.A., et al., 2011. Remotely sensed L-band sar data for tropical forest biomass estimation. Journal of Tropical Forest Science 23, 318–327.

Harris, N.L., Brown, S., Hagen, S.C., Saatchi, S.S., Petrova, S., Salas, W., Hansen, M.C., Potapov, P.V., Lotsch, A., 2012. Baseline map of carbon emissions from deforestation in tropical regions. Science 336, 1573–1576.

Hijmans, R., Cameron, S., Parra, J., Jones, P., Jarvis, A., 2005. Very high resolution interpolated climate surface for global land areas. International journal of climatology , 1965–1978.

Hoekman, D., Quiriones, M., 2000. Land cover type and biomass classification using AIRSAR data for evaluation of monitoring scenarios in the Colombian Amazon. Geoscience and Remote Sensing, IEEE Transactions on 38, 685–696.

Houghton, R., 1999. The annual net flux of carbon to the atmosphere from changes in land use 1850–1990. Tellus B 51, 298–313.

Houghton, R., Hall, F., Goetz, S.J., 2009. Importance of biomass in the global carbon cycle. Journal of Geophysical Research: Biogeosciences (2005–2012) 114.

Imhoff, M.L., 1995. Radar backscatter and biomass saturation: ramifications for global biomass inventory. Geoscience and Remote Sensing, IEEE Transactions on 33, 511–518.

Ishimaru, A., 1978. Wave propagation and scattering in random media. volume 1. Academic Press.

Le Toan, T., Beaudoin, A., Riom, J., Guyon, D., 1992. Relating forest biomass to SAR data. Geoscience and Remote Sensing, IEEE Transactions on 30, 403–411.

Le Toan, T., Quegan, S., Davidson, M., Balzter, H., Paillou, P., Papathanassiou, K., Plummer, S., Rocca, F., Saatchi, S., Shugart, H., et al., 2011. The BIOMASS mission: Mapping global forest biomass to better understand the terrestrial carbon cycle. Remote sensing of environment 115, 2850–2860.

Le Toan, T., Quegan, S., Woodward, I., Lomas, M., Delbart, N., Picard, G., 2004. Relating radar remote sensing of biomass to modelling of forest carbon budgets. Climatic Change 67, 379–402.

Lefsky, M.A., Harding, D.J., Keller, M., Cohen, W.B., Carabajal, C.C., Espirito-Santo, F.D.B., Hunter, M.O., de Oliveira Jr, R., 2005. Estimates of forest canopy height and aboveground biomass using ICESat. Geophysical Research Letters 32, L22S02.

Lewis, S., Lopez-Gonzalez, G., Sonké, B., Affum-Baffoe, K., Baker, T., Ojo, L., Phillips, O., Reitsma, J., White, L., Comiskey, J., et al., 2009. Increasing carbon storage in intact African tropical forests. Nature 457, 1003–1006.

Lucas, R., Armston, J., Fairfax, R., Fensham, R., Accad, A., Carreiras, J., Kelley, J., Bunting, P., Clewley, D., Bray, S., et al., 2010. An evaluation of the ALOS PALSAR L-band backscatter - Above ground biomass relationship - Queensland, Australia: Impacts of surface moisture condition and vegetation structure. Selected Topics in Applied Earth Observations and Remote Sensing, IEEE Journal of 3, 576–593.

Lucas, R., Mitchell, A., Rosenqvist, A., Proisy, C., Melius, A., Ticehurst, C., 2007. The potential of L-band SAR for quantifying mangrove characteristics and change: case studies from the tropics. Aquatic conservation: marine and freshwater ecosystems 17, 245–264.

Mascaro, J., Asner, G.P., Davies, S., Dehgan, A., Saatchi, S., 2014. These are the days of lasers in the jungle. Carbon balance and management 9, 1–3.

Mermoz, S., Le Toan, T., Villard, L., Réjou-Méchain, M., Seifert-Granzin, J., 2014. Biomass assessment in the cameroon savanna using ALOS PALSAR data. Remote Sensing of Environment, In press.

Mitchard, E., Saatchi, S., Gerard, F., Lewis, S., Meir, P., 2009. Measuring woody encroachment along a forest-savanna boundary in Central Africa. Earth Interactions 13.

Mitchard, E., Saatchi, S., Lewis, S., Feldpausch, T., Woodhouse, I., Sonke, B., Rowland, C., Meir, P., 2011. Measuring biomass changes due to woody encroachment and deforestation/degradation in a forest-savanna boundary region of Central Africa using multi-temporal L-band radar backscatter. Remote Sensing of Environment .

Mitchard, E.T., Saatchi, S.S., Baccini, A., Asner, G.P., Goetz, S.J., Harris, N., Brown, S., 2013. Uncertainty in the spatial distribution of tropical forest biomass: a comparison of pan-tropical maps. Carb Bal Manage .

Morel, A.C., Saatchi, S.S., Malhi, Y., Berry, N.J., Banin, L., Burslem, D., Nilus, R., Ong, R.C., 2011. Estimating aboveground biomass in forest and oil palm plantation in Sabah, Malaysian Borneo using ALOS PALSAR data. Forest Ecology and Management 262, 1786–1798.

Morton, D.C., Nagol, J., Carabajal, C.C., Rosette, J., Palace, M., Cook, B.D., North, P.R., 2014. Amazon forests maintain consistent canopy structure and greenness during the dry season. Nature , 1104–1106.

Ploton, P., Pélissier, R., Proisy, C., Flavenot, T., Barbier, N., Rai, S., Couteron, P., 2012. Assessing aboveground tropical forest biomass using Google Earth canopy images. Ecological Applications 22, 993–1003.

Proisy, C., Couteron, P., Fromard, F., 2007. Predicting and mapping mangrove biomass from canopy grain analysis using fourier-based textural ordination of IKONOS images. Remote Sensing of Environment 109, 379–392.

Ramankutty, N., Gibbs, H.K., Achard, F., Defries, R., Foley, J.A., Houghton, R., 2007. Challenges to estimating carbon emissions from tropical deforestation. Global Change Biology 13, 51–66.

Réjou-Méchain, M., Fayolle, A., Nasi, R., Gourlet-Fleury, S., Doucet, J., Gally, M., Hubert, D., Pasquier, A., Billand, A., 2011. Detecting large-scale diversity patterns in tropical trees: Can we trust commercial forest inventories? Forest Ecology and Management 261, 187–194.

Réjou-Méchain, M., Muller-Landau, H.C., Detto, M., Thomas, S.C., Le Toan, T., Saatchi, S.S., Barreto-Silva, J.S., Bourg, N.A., Bunyavejchewin, S., Butt, N., Brockelman, W.Y., Cao, M., Cárdenas, D., Chiang, J.M., Chuyong, G.B., Clay, K., Condit, R., Dattaraja, H.S., Davies, S.J., Duque, A., Esufali, S., Ewango, C., Fernando, R.H.S., Fletcher, C.D., Gunatilleke, I.A.U.N., Hao, Z., Harms, K.E., Hart, T.B., Hérault, B., Howe, R.W., Hubbell, S.P., Johnson, D.J., Kenfack, D., Larson, A.J., Lin, L., Lin, Y., Lutz, J.A., Makana, J.R., Malhi, Y., Marthews, T.R., McEwan, R.W., McMahon, S.M., McShea, W.J., Muscarella, R., Nathalang, A., Noor, N.S.M., Nytch, C.J., Oliveira, A.A., Phillips, R.P., Pongpattananurak, N., Punchi-Manage, R., Salim, R., Schurman, J., Sukumar, R., Suresh, H.S., Suwanvecho, U., Thomas, D.W., Thompson, J., Uríarte, M., Valencia, R., Vicentini, A., Wolf, A.T., Yap, S., Yuan, Z., Zartman, C.E., Zimmerman, J.K., Chave, J., 2014. Local spatial structure of forest biomass and its consequences for remote sensing of carbon stocks. Biogeosciences Discussions 11, 5711–5742.

Saatchi, S., Halligan, K., Despain, D., Crabtree, R., 2007. Estimation of forest fuel load from radar remote sensing. Geoscience and Remote Sensing, IEEE Transactions on 45, 1726–1740.

Saatchi, S., Marlier, M., Chazdon, R., Clark, D., Russell, A., 2011. Impact of spatial variability of tropical forest structure on radar estimation of aboveground biomass. Remote Sensing of Environment , 2836–2849.

Sandberg, G., Ulander, L., Fransson, J., Holmgren, J., Toan, T.L., 2011. L- and P-band backscatter intensity for biomass retrieval in hemiboreal forest. Remote Sensing of Environment 115, 28742886.

Santoro, M., 2003. Estimation of biophysical parameters in boreal forests from ERS and JERS SAR interferometry. Ph.D. thesis. Department of Radio and Space Science, Chalmers University of Technology.

Santos, J., Lacruz, M., Araujo, L., Keil, M., 2002. Savanna and tropical rainforest biomass estimation and spatialization using JERS-1 data. International Journal of Remote Sensing , 1217–1229.

Sexton, J.O., Song, X.P., Feng, M., Noojipady, P., Anand, A., Huang, C., Kim, D.H., Collins, K.M., Channan, S., DiMiceli, C., et al., 2013. Global, 30-m resolution continuous fields of tree cover: Landsat-based rescaling of modis vegetation continuous fields with lidar-based estimates of error. International Journal of Digital Earth 6, 427–448.

Shimada, M., Isoguchi, O., T., T., Isono, K., 2009. PALSAR radiometric and geometric calibration. Geoscience and Remote Sensing, IEEE Transactions on 47, 3915–3932.

Shimada, M., Ohtaki, T., 2010. Generating large-scale high-quality sar mosaic datasets: application to PALSAR data for global monitoring. Geoscience and Remote Sensing, IEEE Transactions on 3, 637–656.

Shugart, H., Saatchi, S., Hall, F., 2010. Importance of structure and its measurement in quantifying function of forest ecosystems. Journal of Geophysical Research: Biogeosciences (2005–2012) 115.

Van Zyl, J.J., Chapman, B.D., Dubois, P., Shi, J., 1993. The effect of topography on SAR calibration. Geoscience and Remote Sensing, IEEE Transactions on 31, 1036–1043.

Vancutsem, C., Pekel, J.F., Evrard, C., Malaisse, F., Defourny, P., 2009. Mapping and characterizing the vegetation types of the democratic republic of congo using spot vegetation time series. International Journal of Applied Earth Observation and Geoinformation 11, 62–76.

Verhegghen, A., Mayaux, P., De Wasseige, C., Defourny, P., et al., 2012. Mapping congo basin vegetation types from 300 m and 1 km multi-sensor time series for carbon stocks and forest areas estimation. Biogeosciences 9, 5061–5079.

Viennois, G., Barbier, N., Fabre, I., Couteron, P., 2013. Multiresolution quantification of deciduousness in west-central african forests. Biogeosciences 10, 6957–6967.

Viergever, K.M., 2008. Establishing the sensitivity of Synthetic Aperture Radar to above-ground biomass in wooded savannas. Ph.D. thesis. University of Edinburgh.

Villard, L., 2009. Forward and Inverse Modeling of Synthetic Aperture Radar in the Bistatic Configuration: Applications in Forest Remote Sensing. Ph.D. thesis. ONERA-ISAE-Universite Paul Sabatier.

Zolkos, S., Goetz, S., Dubayah, R., 2013. A meta-analysis of terrestrial aboveground biomass estimation using lidar remote sensing. Remote Sensing of Environment 128, 289–298.

List of Figures

Appendix A. Forest growth model used for electromagnetic simulations

The forest growth model (Figure 2) has been developed to model all the geometrical parameters required for the EM calculations (in the MIPERS model) as a function of forest AGB. The first step turns the input AGB into forest total height (trunk+crown) based on the allometric equation proposed in Asner et al. (2012) for forests in Peru.

Wood density, which is essential in the MCH to AGB relationship and to turn biomass values in terms of the geometrical parameters describing the modelled forest, has been kept constant given the poor correlation with forest AGB. However, the impact of the dispersion around the mean value (0.58) is shown in Figure 3 (filled colour domains).

The allometric equations (2) and (3) in Figure 2 are used to compute DBH and BA. Equation (2) has been formulated from tree height. Likewise, the number of trunk per hectare N_t has been estimated with the hypothesis of a trunk layer composed of a single class of DBH (the DBH of all the trunks is constant), so that N_t is simply deduced from DBH and BA. Such an approximation is limiting to generalize our modelling approach to several tropical forests (for which various classes of DBH would better match the various populations of trunks). For example, this DBH approximation leads to unrealistic numbers of trunks per hectare in the other test sites used in Asner et al. (2012) (Panama, Hawaii and Madagascar). More complex forest growth models have been developed to overcome this limitation but are not yet published, and their description would require many details in this paper, in which the EM simulations have not been used to draw universal theoretical laws but to support and explain our experimental results.

The crown height h_t varies linearly from approximately 60% to 75% with increasing forest biomass. Considering conical cylinders for the trunks to account for the tapering factor, the total AGB can be formulated as follows :

$$\begin{aligned} AGB[t/ha] =& AGB_t[t/ha] + AGB_c[t/ha] \\ =& N_t \cdot \rho \cdot \frac{\pi}{3} h_t \big(r_{BA}^2 + r_{BA} r_t + r_t^2 \big) + \rho\pi \big(\sum_i N_i r_i^2 h_i \big) \end{aligned} \tag{A.1}$$

where r_t is the radius of the trunks at the top of the trunk layer. The remaining geometrical parameters concern the branches (classes 3 and 4) within the crown layer, which are deduced from their upper class, based on the branching rules governed by surface conservation (commonly referred to as the pipe model).

Appendix B. Details on the above ground biomass calculation and errors propagation

Appendix B.1. Wood specific gravity

We used the African wood specific gravity (WSG) dataset of Gourlet-Fleury et al. (2011) to assign a WSG value to each tree. This dataset was based on 1206 trees belonging to 256 African species and on 29 additional species identified to the genus level. For each taxa, the assignment rules of Gourlet-Fleury et al. (2011) give a mean WSG values per taxa at the species, the genus, the family, the order or the global levels. A variance associated with each WSG estimate was calculated using repeated WSG values within taxa levels (Gourlet-Fleury et al., 2011). Overall, 55.6 % of the individuals had a WSG attributed at the species level, 0.2 % at the genus level, 14.2 % at the family level, 20.3 % at the order level and 9.8% at the global level.

Appendix B.2. Tree diameter

In the original forest inventory, the trees were allocated into diameter classes. However, the biomass allometry used needs the exact DBH of the trees. Thus, we assumed an exponential distribution for the tree diameters. We estimated the parameter of the exponential distribution, α, by minimizing the sum of the absolute differences between the proportion of trees inventoried in each diameter class (with the last class=[190 ∞[) and the proportions of trees expected by the exponential distribution ($\alpha = 0.0622$ cm^{-1}). Then, for a tree in a given diameter class, we used the exponential distribution of parameter truncated to its diameter class. For example, a tree with its DBH in the class [30 40[has a diameter distribution defined by

$$\mathscr{F}(DBH) = \frac{e^{-\alpha.DBH}}{\int_{30}^{40} e^{-\alpha.DBH} dDBH}.I_{[30\ 40]}(DBH) \quad \text{(B.1)}$$

with $I_{[30\ 40]}(DBH) = 1$ if the DBH is [30 40[and 0 otherwise.

Appendix B.3. Tree height

Height-diameter allometry varies strongly among tropical regions: for a given diameter, a high variability of tree height occurs according to the region considered. To minimize this potential bias, we used a regional specific height-diameter model based on 2,572 measured trees in central Africa (Feldpausch et al., 2012):

$$H = 50.453(1 - e^{-0.0471.DBH^{0.812}}) \quad \text{(B.2)}$$

where H is the estimated tree height and DBH is the diameter at breast height estimated from the fitted truncated exponential function.

Appendix B.4. AGB estimation and uncertainties

To estimate both the mean AGB per 0.5-ha field plot, $\mu_{AGB,plot}$, and the AGB variance, $\sigma^2_{AGB,plot}$, we built a Monte Carlo scheme with 1,000 simulations per plot. During the simulations, WSG values were first picked randomly and independently for each tree from the normal distribution $\mathcal{N}(\mu_{WSG}, \sigma_{WSG})$ where μ_{WSG} and σ_{WSG} are, respectively, the mean and the standard deviation of the WSG values for a given taxa (see Appendix B.1). The DBH of each tree was drawn randomly from the exponential function between the two boundaries of its diameter classes (see Appendix B.2). The tree height was then estimated from these DBH values as follows:

$$H = 50.453(1 - e^{-0.0471.DBH^{0.812}}) + \epsilon_H \tag{B.3}$$

where ϵ_H is a random error drawn from a normal distribution, with 6.177 being the residual standard error (RSE) of the height-diameter model provided in Feldpausch et al. (2012). The AGB values were then calculated independently for each tree and at each simulation using the model of Chave et al. (2005):

$$AGB = e^{-3.027+log(WSG.DBH^2.H)+\epsilon_{AGB}} \tag{B.4}$$

where ϵ_{AGB} is a random error drawn from a normal distribution $\mathcal{N}(0, 0.316)$, with 0.316 being the RSE of the AGB model provided in Chave et al. (2005).

For each 0.5-ha field plot, we finally calculated $\mu_{AGB,plot}$ and $\sigma^2_{AGB,plot}$, as the mean and the variance of the 1000 AGB estimates per plot respectively. These field plots AGB estimates $\mu_{AGB,plot}$ were then averaged in a pixel of 1 km resolution to obtain upscaled plots, and the standard deviation associated with a pixel AGB value, $\sigma^2_{AGB,pixel}$, was calculated as follows:

$$\sigma^2_{AGB,pixel} = E(\sigma^2_{AGB,plot}) + \sigma^2(\mu_{AGB,plot}) \tag{B.5}$$

where $\sigma^2(\mu_{AGB,plot})$ is the variance of the plot-based AGB values $\mu_{AGB,plot}$ contained in the pixel.

Appendix C. Details on the reduction of the uncertainties

Appendix C.1. Uncertainties from the coefficient of variations among the field plots

The effects of the CV among the field plots within each upscaled plot on the relationship between SAR backscatter and AGB are quantified for CVs ranging from 0.1 to 0.5. Upscaled plots with the standard deviation of the backscatter $>$ 1 dB and slope median $> 5^o$ were discarded. The best linear regressions are performed each time at HH and HV polarizations. The resulting r and biases are shown in Figure C.1 and are associated with the number of pixels used to compute the fits (vertical solid bars). Both γ^o_{HH} and γ^o_{HV} show decreasing r (from 0.39 to 0.21 and from 0.35 to 0.20, respectively) and slightly increasing biases (from 0.12 to 0.14 dB independent of the polarization) with an increase in the AGB CV. When CV< 0.25, γ^o_{HH} was found to provide the best fit and a smaller bias. The trends start to saturate when the CV is over 0.4. The threshold of 0.25 has been chosen to ensure that the slope of the regressions and the Pearson correlations were acceptable while keeping a significant amount of pixels. A more drastic selection would discard almost all the pixels.

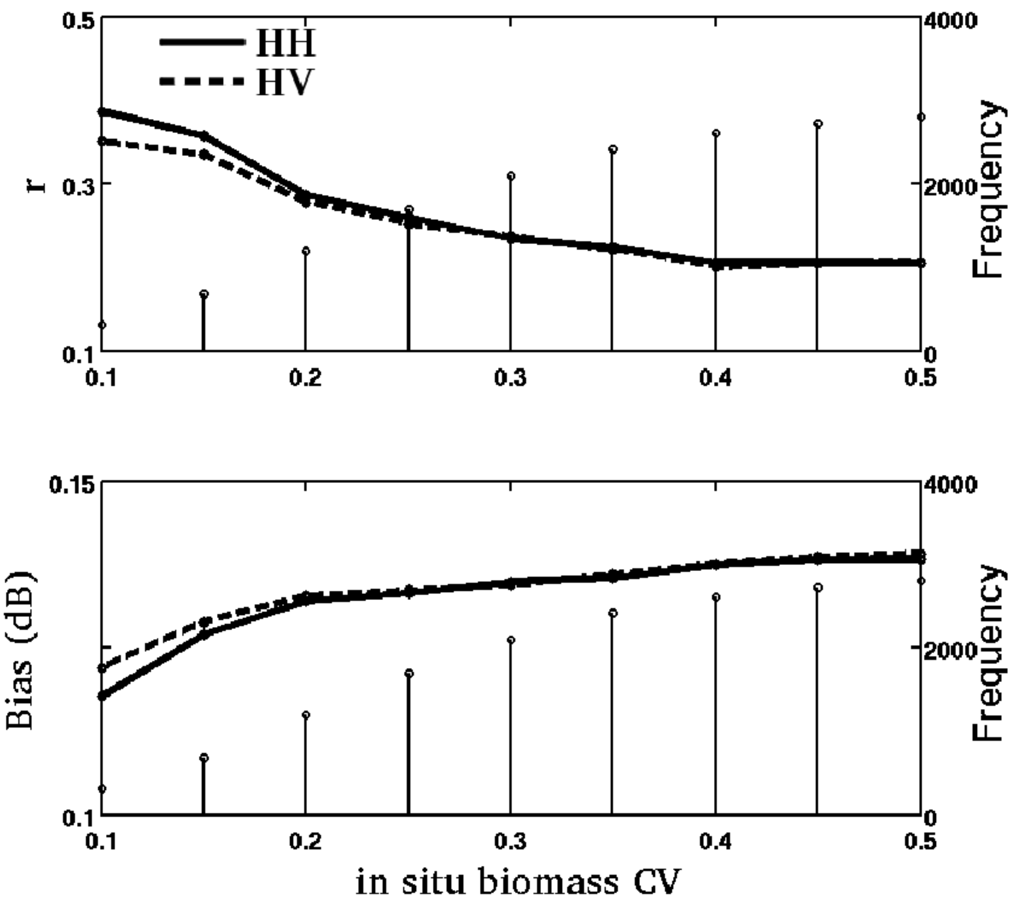

Figure C.1: Effects of the coefficients of variation (CV) among the field plots within each upscaled plot on the radar sensitivity to above ground biomass (AGB): r and bias are shown in figures at the top and bottom, respectively. The frequencies of the remaining upscaled plots are indicated by vertical solid bars.

Appendix C.2. Uncertainties from topography

The effects of terrain slope on the relationship between radar backscatter and AGB are assessed, with slope medians ranging from 0.25 to 2.50^o. We filtered out upscaled plots with CV > 0.25 and standard deviations of the backscatter > 1 dB. The quantitative results are shown in Figure C.2. Both γ^o_{HH} and γ^o_{HV} show a decreasing r (from 0.45 to 0.22 and from 0.39 to 0.22, respectively) and an increasing bias (from 0.11 to 0.14 dB independent of the polarization) with an increase in the slope median. When the slope median $< 5^o$, γ^o_{HH} was found to provide the best fit and a slightly larger bias. The trends start to saturate when the slope median is over 6^o.

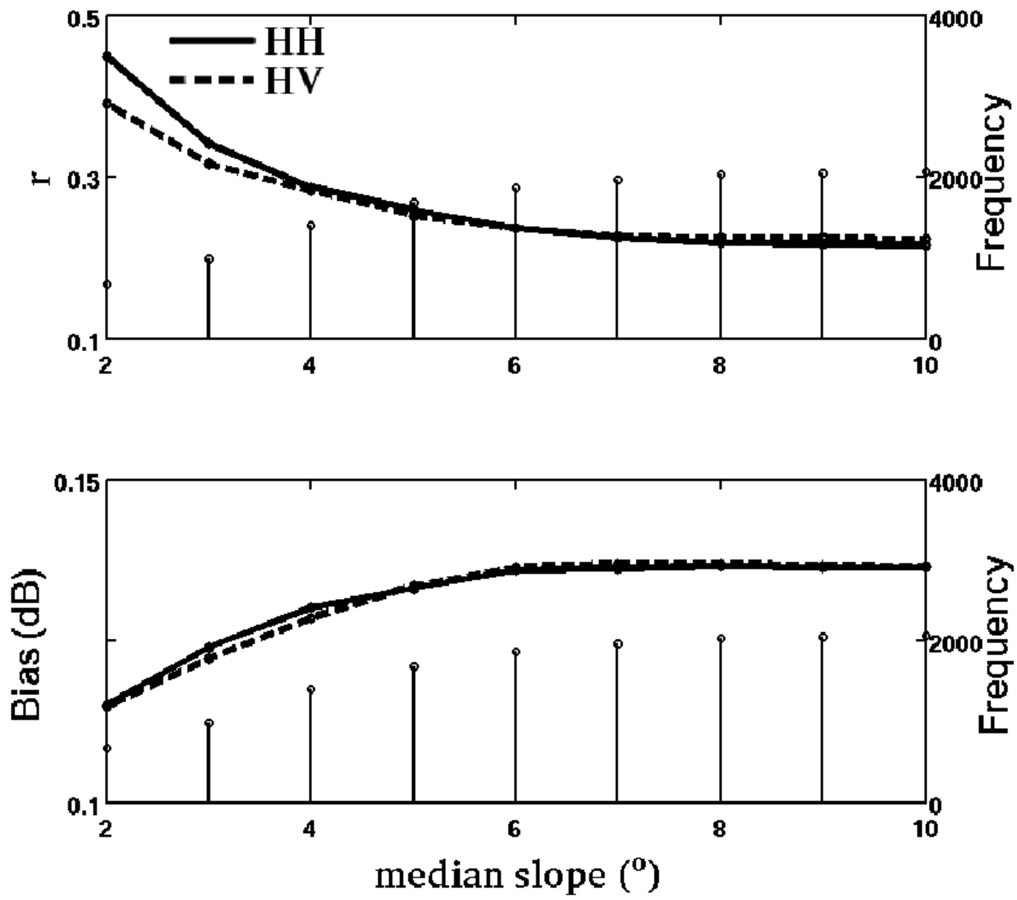

Figure C.2: Effects of the median of terrain slope on the radar sensitivity to above ground biomass (AGB): r and bias are shown in figures at the top and bottom, respectively. The frequencies of the remaining upscaled plots are indicated by vertical solid bars.